

Demonstration of the QCCD trapped-ion quantum computer architecture

J. M. Pino,* J. M. Dreiling, C. Figgatt, J. P. Gaebler, S. A. Moses, M. S. Allman, C. H. Baldwin, M. Foss-Feig, D. Hayes, K. Mayer, C. Ryan-Anderson, and B. Neyenhuis
Honeywell Quantum Solutions, 303 S. Technology Ct., Broomfield, Colorado 80021, USA
(Dated: August 26, 2021)

The trapped-ion QCCD (quantum charge-coupled device) architecture proposal [1, 2] lays out a blueprint for a universal quantum computer. The design begins with electrodes patterned on a two-dimensional surface configured to trap multiple arrays of ions (or ion crystals). Communication within the ion crystal network allows for the machine to be scaled while keeping the number of ions in each crystal to a small number, thereby preserving the low error rates demonstrated in trapped-ion experiments [3–5]. By proposing to communicate quantum information by moving the ions through space to interact with other distant ions, the architecture creates a quantum computer endowed with full-connectivity. However, engineering this fully-connected computer introduces a host of difficulties that have precluded the architecture from being fully realized in the twenty years since its proposal. Using a Honeywell cryogenic surface trap, we report on the integration of all necessary ingredients of the QCCD architecture into a programmable trapped-ion quantum computer. Using four and six qubit circuits, the system level performance of the processor is quantified by the fidelity of a teleported CNOT gate utilizing mid-circuit measurement [6] and a quantum volume measurement of $2^6 = 64$ [7]. By demonstrating that the low error rates achievable in small ion crystals can be successfully integrated with a scalable trap design, parallel optical delivery, and fast ion transport, the QCCD architecture is shown to be a viable path toward large quantum computers. Atomic ions provide perfectly identical, high-fidelity qubits. Our work shows that the QCCD architecture built around these qubits will provide high performance quantum computers, likely enabling important near-term demonstrations such as quantum error correction and quantum advantage.

The first quantum logic gates were performed with trapped ions [8, 9], and since then, researchers have demonstrated coherence times and gate, state preparation, and measurement fidelities surpassing those of other competing quantum computing architectures [3–5, 10]. More recently, researchers have focused their attention toward scaling to the large number of qubits needed for complex quantum algorithms. While small trapped-ion quantum computers may only require a single trapping region with the ions in a single crystal, this approach is unlikely to scale to very large numbers of qubits. Efforts have therefore focused on architectures that use a network of ion crystals that are connected through photonic links [11, 12] or physically transporting ions between dif-

ferent crystals. Here we demonstrate the latter approach.

The QCCD architecture aims to create a fully connected, high fidelity, and scalable quantum computer, but it does so at the cost of some challenging requirements: **1** – a device capable of trapping a large number of small ion crystals, **2** – fast transport operations for reordering and precise positioning of ions, **3** – clock synchronization across different trapping regions, **4** – the likely need for trapping two different ion species, one used as a qubit and another for sympathetic cooling, and **5** – parallelization of transport and quantum operations across the device. Many of the difficulties have been addressed individually [13–17], but combining these features into a single machine creates performance requirements that are seemingly at odds and greatly increases the need for automation and robustness. In this article, we report on the integration of all these ingredients and demonstrate that all individual components operate with low error rates, cross-talk errors are small, the system is capable of mid-circuit measurements and conditioned feed-back, and that the system as a whole operates faithfully so as to maximize the quantum volume[7] of the device for up to six qubits.

Requirement **1** in the architecture is an ion trap capable of quickly rearranging ion crystals to enable different quantum operations. The ion trap at the heart of the quantum computer shown in Fig. 1 has a linear geometry set by RF electrodes (colored green in Fig. 1b) that provide a uniform radial trapping force along a line $70\mu\text{m}$ above the surface (called the RF-null). The more complex trapping potentials and transport capabilities are provided by the segmented DC electrodes. The geometry is flexible enough to admit different modes of operation, but we limit our description to the simplest case where the trap is understood as consisting of sixteen different *zones* and identified in Fig. 1 as gate (blue), storage (orange), auxiliary (yellow) and loading (pink) zones. Only the gate and storage zones are suitable for complex transport operations, making them the most convenient for quantum operations. Here, we use the storage zone closest to the loading hole as a gate zone for convenience (Fig. 4) and refer to it as a gate zone for ease of reference.

Quantum logic operations are executed in the gate zones using lasers propagating parallel to the trap surface. The beams are focused tightly enough to address a single zone but not tight enough to allow for individual addressing within a single ion crystal. This means that entangling operations between arbitrary pairs, single-

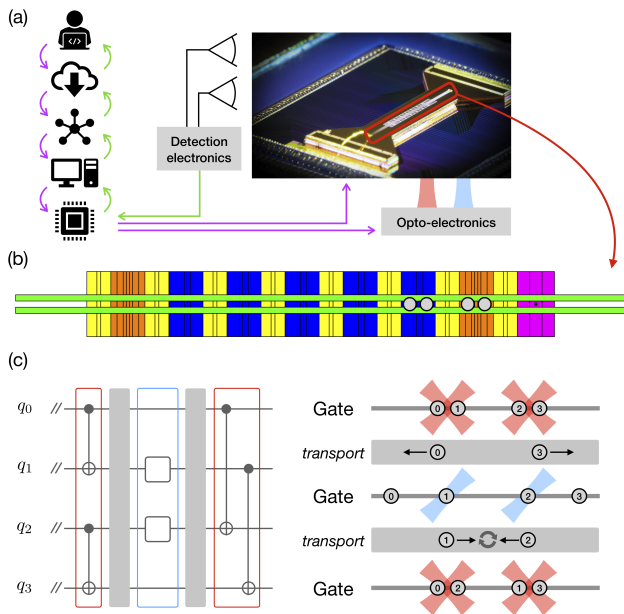


FIG. 1. The programmable QCCD quantum computing system. (a) Right, a picture of the trap. Left, the information flow from the user to the trapped qubits. From top to bottom, we illustrate: user, cloud, internal tasking, machine control system, FPGA. The circuits are processed by a compiler to generate control signals (purple) sent to both the trap and optoelectronic devices that control laser beams. An imaging system and PMT array collect and count scattered photons, and the result (green) is sent back to the software stack and user. (b) A schematic of the trap: RF electrodes (green), loading hole (black), load zone (pink), storage zones (orange), gate zones (blue), and auxiliary zones (yellow) for qubit storage. (c) A general quantum circuit: ions already sharing a gate zone are gated, then spatially isolated for single-qubit gates, then the second and third ions are swapped for the final two-qubit gates. While not shown, readout, two-qubit gates, and single-qubit rotations can all be performed in parallel.

qubit operations, measurement, and reset all require crystal rearrangement.

In this article, we limit the modes of operation to either $N = 4$ or $N = 6$ qubits, always matching the number of $^{171}\text{Yb}^+$ qubit ions and $^{138}\text{Ba}^+$ coolant ions. The machine is initialized differently depending on what mode of operation is being used, but all quantum circuits begin by grouping the ions into either four-ion crystals (Ba-Yb-Yb-Ba) or two-ion crystals (Yb-Ba) in the various zones. Ions are also grouped this way during a computation, but are additionally grouped as Yb-Ba-Ba-Yb. The $N = 4$ mode makes minimal use of the auxiliary zones, using them only for transport between gating operations, whereas the $N = 6$ mode utilizes the auxiliary zones as quantum memories while logic operations are occurring in the gating regions.

A quantum computation begins with a user submitting a program in the form of a quantum circuit. A compiler assigns qubits to physical ions so as to mini-

mize the number of transport operations needed and the circuit proceeds as a series of transport and gating operations, pairing and isolating qubits appropriately for entangling operations, single-qubit operations and measurements. After completing all of the quantum operations, the ions are returned to the initial configuration so that the circuit can be repeated to gather statistics before sending the results back to the user.

A striking feature of the QCCD architecture is the ability to perform a logic gate between any two qubits, significantly reducing the computational overhead compared to architectures without all-to-all connectivity. This ability is made possible by the long coherence time of atomic clock states used for the qubit along with the fact that the electric fields used for transport do not couple to the internal degrees of freedom of the ions. The transport that enables all-to-all connectivity (requirement 2) is achieved through dynamic voltage waveforms applied to the DC electrodes and they fall into three categories:

Linear transport: A potential well is moved along the RF null from one region of the trap to another [18]. During a quantum computation, these operations can be done in parallel with multiple wells at different positions being moved simultaneously. Except during initialization procedures, these linear transports always involve moving a Yb-Ba pair.

Split/combine: A split operation divides a single potential well into two [19], splitting a 4-ion crystal into two 2-ion crystals. The combine operation is the time reversal of the split operation, and both occur only in the gate zones.

Swap: The qubit order of a 4-ion crystal is flipped by rotating the qubits about an axis perpendicular to the RF null [20]. These operations only occur in gate zones.

As described in the Methods section, these operations take between 50 and 300 μs and can be done without introducing a large amount of heat into the system as shown in Table II. The three transport primitives are used to execute a parallel bubble, or odd-even, sorting algorithm that can sort an array of length N in $\mathcal{O}(N)$ steps [21], and can therefore rearrange the qubits arbitrarily. The transport sequences can involve several operations for every quantum logic operation as illustrated in Fig. 2. Transport failure events are rare and are automatically detected and scrubbed from the data sets so that computations are not corrupted.

Clock synchronization across the spatially separated interaction zones (requirement 3) implies the need for both stable qubits and phase stable gate operations. To this end, we use the hyperfine "clock" states in the $^2S_{1/2}$ ground state of $^{171}\text{Yb}^+$ as the qubit and define $|0\rangle \equiv |F = 0, m_F = 0\rangle$ and $|1\rangle \equiv |F = 1, m_F = 0\rangle$, where F and m_F are the quantum numbers for total angular momentum and its z-projection. These states have naturally long coherence times due to their first order insensitivity to magnetic field fluctuations and we measure a spin-echo

T2 of approximately 2 s in both interaction zones.

Our native gate set consists of four types of phase stable gates (see Methods for more details):

Single-qubit (SQ) Z rotations: The single-qubit rotation around Z is done entirely in software by a phase-tracking update as described in the Methods section. We set a resolution limit of $\pi/500$ for Z rotations.

Single-qubit X/Y rotations: Stimulated Raman transitions on an isolated Yb-Ba crystal apply single-qubit rotations about an arbitrary axis in the X - Y plane of the Bloch sphere. We currently restrict our gate set to π and $\pi/2$ rotations. Arbitrary single-qubit gates submitted by the user are synthesized into at most two X/Y rotations along with an additional Z -rotation. These gates are only sensitive to the microwave phase of the qubit and do not require optical phase stability.

Two-qubit (TQ) gates: We operate a Mølmer-Sørensen interaction [22] in the phase-sensitive configuration [23, 24] and add single-qubit wrapper pulses driven with the same lasers (Fig. 5) to remove the optical phase dependence, resulting in the phase-insensitive entangling gate $U_{zz} = \exp(-i\frac{\pi}{4}Z \otimes Z)$. Removing the optical phase sensitivity of the gate is crucial to having clock synchronized gate zones.

Global microwave rotations: A microwave antenna in the vacuum chamber applies global qubit rotations with a variable phase. The microwave field amplitude has a 3% inhomogeneity across the device and, therefore, is not suitable for logical operations, nor is it available to be used in quantum circuits. However, microwaves are used to suppress memory errors through dynamical decoupling [25]. Since the amplitude is inhomogeneous, we cannot apply global microwave π pulses, as is the nominal prescription for dynamical decoupling. To avoid the accumulation of coherent errors, we apply pulses in pairs with opposite phases during ground-state cooling without any transport operation in between, thereby canceling out the small amplitude errors while preserving most of the memory error suppression benefits.

Qubit initialization and measurement are done by spatially isolating a single Yb-Ba crystal so that resonantly scattered light has a minimal effect on the other qubits, allowing measurement (and subsequent reinitialization, if necessary) to be performed at any point in the circuit. We use standard optical pumping and state-dependent fluorescence procedures for the initialization and measurement protocols [26] (see Methods section for more details).

Aside from the global microwave operations, these quantum operations are characterized in both gate zones using RB (randomized benchmarking) techniques [27]. The similar environments for the two zones result in nearly identical operation times and fidelities which are summarized in Table I and Table III and an estimated error budget for two-qubit gates is given in Table IV in the Methods section.

As mentioned before, we meet the sympathetic cooling requirement (4) with $^{138}\text{Ba}^+$ as the coolant ion and employ both Doppler and resolved sideband cooling [28] at various times throughout a quantum circuit, (see Methods section for details). The cooling laser light is tuned near the Ba transition at 493.5 nm, which is far enough from any resonances in Yb to prevent any induced errors. These cooling protocols are the current runtime bottlenecks in our device (Fig. 2b, Fig. 9, Fig. 10) and are likely necessary for the QCCD architecture but can be significantly improved [29].

The final requirement 5 of parallelized quantum operations and transport is verified at the system level through holistic benchmarks. We performed three holistic measurements aimed at characterizing the system performance as a general quantum information processor. The first benchmark performed is simultaneous benchmarking in the different gate zones, the second is a teleported CNOT gate using mid-circuit measurements, and the third is a measurement of the system's quantum volume.

Simultaneous RB is performed with single and two-qubit gates to measure the performance in each gate zone with $N = 4$ qubits. We also generalized the single-qubit simultaneous RB method [30] to two-qubits to detect cross-talk errors. As described in detail in the Methods section, this benchmark works by performing RB tests separately in each zone, then simultaneously in the two zones and extracting addressability and correlation error signals. As summarized in Table V and Fig. 7, we find the cross-talk errors to be negligible in this system, highlighting another advantage of the QCCD architecture using spatially separated interaction zones addressed by localized laser beams.

Splitting and spatially isolating ion crystals enable measurement of a single qubit in the middle of a circuit without damaging the quantum information stored in the other qubits. Recently, the NIST group demonstrated mid-circuit measurements through a teleported CNOT gate circuit [6], which we use as our algorithmic benchmark for this primitive. As described in the Methods section, quantum gate teleportation is a protocol for applying a gate between a pair of remote data qubits [31] and requires entangling operations, mid-circuit measurements, and classically-conditioned quantum gates - all of which are necessary for quantum error correction. The protocol uses four qubits and through a combination of three entangling operations, two mid-circuit measurements and two measurement conditioned single-qubit operations, the protocol executes a quantum CNOT gate between two qubits that never directly interact with each other. By evaluating all four input states in two different bases (eight total input states), we lower bound the fidelity of the operation to be $F_{\text{avg}} \geq 0.899(6)$. This constitutes the first demonstration of a full-stack quantum computer capable of high-fidelity mid-circuit mea-

Component	Zone Avg.	Zone 1	Zone 2
SPAM (simultaneous SQ RB)	$3(1) \times 10^{-3}$	$[3(1) \times 10^{-3}, 3(1) \times 10^{-3}]$	$[2(1) \times 10^{-3}, 3(1) \times 10^{-3}]$
Single-qubit gates (simultaneous RB)	$1.1(3) \times 10^{-4}$	$[1.4(3) \times 10^{-4}, 1.2(2) \times 10^{-4}]$	$[9(2) \times 10^{-5}, 1.0(3) \times 10^{-4}]$
Two-qubit gates (individual RB)	$7.9(4) \times 10^{-3}$	$6.7(5) \times 10^{-3}$	$9.0(4) \times 10^{-3}$
Two-qubit gates (simultaneous RB)	$8.0(4) \times 10^{-3}$	$7.2(4) \times 10^{-3}$	$8.8(4) \times 10^{-3}$

TABLE I. Component benchmarking results. Numbers are the average error per operation. For SPAM and single-qubit gates, the two numbers represent the measured values for each qubit in the corresponding zone using the high-fidelity ($120 \mu\text{s}$ duration) detection.

surement and feedback operations.

Quantum volume (QV) is a full-circuit benchmark dependent on qubit number, gate fidelity and connectivity, and attempts to estimate the effective power of the quantum computer [7] and is sensitive to errors that may be missed by component benchmarks. A QV test consists of running random $O(N)$ depth circuits with N qubits, as shown in Fig. 3a for $N = 4$. The circuits are then classically simulated, and the measured outputs are tested against the heavy-outcome criteria. If the circuits pass this test $2/3$ of the time with two sigma confidence, then the system is said to have $\text{QV} = 2^N$.

As detailed in the Methods section, we performed QV tests on $N = 2, 3, 4$ and 6 qubits and passed in all cases: for $N = 2$ with 77.58% of the circuits and 99.56% confidence, $N = 3$ with 83.28% of the circuits with 99.9996% confidence, $N = 4$ with 76.77% of the circuits and 99.16% confidence, and $N = 6$ with 72.96% and 99.77% confidence (results are plotted in Fig. 3b).

Fig. 3b also shows theoretical simulations of the circuit outcomes assuming a depolarizing noise channel for the two-qubit gates, with a noise magnitude extracted from two-qubit RB. The excellent agreement provides further evidence that the QCCD architecture fulfills its most ambitious goal: maintaining the gate fidelities achievable in small ion crystals while executing arbitrary circuits on multiple qubits.

We are currently pursuing a scaling of the optical delivery to all five gates zones in our trap, and along with expected fidelity improvements (see below), we expect to increase the accessible quantum volume. The current runtime bottlenecks for the device are the cooling procedures, which can be considerably improved with the combination of improved transport operations [33] and advanced cooling techniques [29]. The current algorithmic bottleneck is the two-qubit gate fidelity, which is consistent with error models pointing to voltage noise in the waveform generators and spontaneous emission as the two dominant error sources. These errors can be mitigated with advanced filtering techniques and larger Raman laser detunings, respectively.

The path to truly large systems of thousands or millions of qubits remains unclear. Our architecture could be scaled in a straight forward manner by placing multiple linear chip-traps end-to-end without major changes in the individual components used. This linear scaling

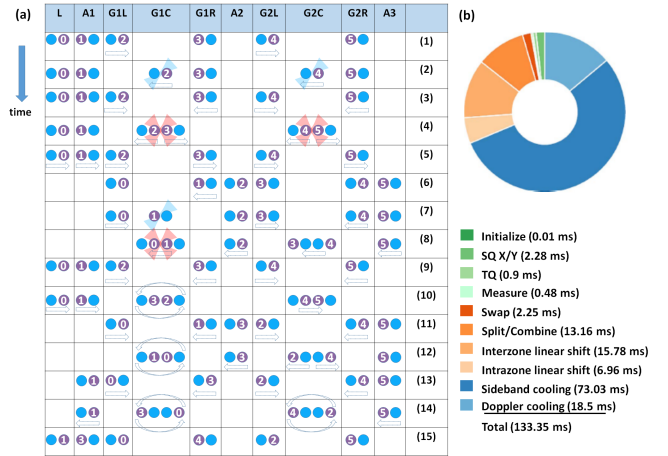


FIG. 2. Transport operations and timing for an $N = 6$ QV test circuit. (a) An example of the transport operations between two $SU(4)$ gates with the random qubit permutation $\Pi = (0, 1, 2, 3, 4, 5) \rightarrow (1, 3, 0, 4, 2, 5)$ (coolant ions are not numbered and cooling steps are not called out). Trap regions are labeled as load zone (L), auxiliary zone 1 (A1), gate zone 1 - left (G1L), gate zone 1 - center (G1C), gate zone 1 - right (G1R), auxiliary zone 2 (A2), gate zone 2 - left (G2L), gate zone 2 - center (G2C) and gate zone 2 - right (G2R). The distance from the center of the gate zone to the left and right regions is $110 \mu\text{m}$. The different steps described in the text are labeled as follows: (1) linear shift, (2) single-qubit gate then linear shift, (3) combine, (4) two-qubit gate then split, (5) linear shift, (6) linear shift, (7) single-qubit gate then combine, (8) two-qubit gate, split then linear shift, (9) combine, (10) swap, split then linear shift, (11) combine, (12) swap, split then linear shift, (13) combine, (14) swap then linear shift. The times for these operations are in Tables II and III. (b) A detailing of the total time spent on the various operations during an $N = 6$ QV circuit. The $N = 6$ QV circuits have approximately 15 random $SU(4)$ gates, compiling down to 45 two-qubit gates.

would result in a linearly increasing transport time for fully connected circuits, which could limit the system's achievable connectivity due to a finite coherence time. Other scaling routes that would better maintain connectivity include using flying qubits (photonic interconnects or ion highways) or a 2D trap geometry. The latter approach requires junction transport and a laser geometry that would avoid beam clipping on a large chip [34, 35].

The question of how to most efficiently move quan-

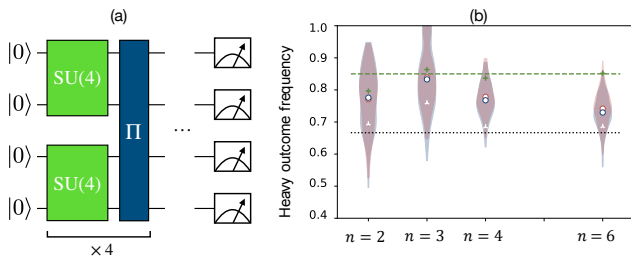


FIG. 3. QV circuits and measurements. (a) The test is run by interleaving random $SU(4)$ gates, each requiring three entangling gates, with random permutations (Π) of qubits (this example illustrates the $N = 4$ case). (b) Results for QV test for $N = 2, 3, 4$, and 6 . Each test was performed with randomly generated circuits from Qiskit [32] with the distribution over circuits plotted in blue. Noisy simulations run in Qiskit with depolarizing errors with rates estimated from RB experiments are plotted in red. Green crosses give the average of the ideal outcomes for the circuits run. The green dashed line is the average over all ideal circuits and the black dashed line shows the passing threshold. The white tri-points show the two-sigma points in the measured distributions.

tum information through a computer is not settled. It is widely expected that large scale quantum computations will require error correction, and it is not yet clear how ion transport may be used to optimize code performance. For example, leveraging high-connectivity is expected to enable more efficient encodings [36] and the true optimal design may ultimately require different connectivities at different scales.

Methods

Honeywell Surface Trap: We designed and fabricated a 2D surface trap at Honeywell’s microfabrication production facility in Plymouth, MN. The trap dimensions given in Fig. 4 result in an ion height of $70 \mu\text{m}$ above the surface. Potential wells are generated by 198 DC gold electrodes which were fabricated with an undercut etch to mitigate stray fields by eliminating a line of sight between dielectrics and the ions [14]. The trap is cooled to 12.6 K via a cold finger attached to a liquid He flow cryostat with stability better than 2 mK, thereby suppressing gate errors due to anomalous heating [37]. We measure single ion axial heating rates (at a 0.97 MHz trap frequency) varying from 100-500 quanta/sec.

Computer Control: The processor is programmed using a quantum circuit [38] that is compiled into hardware commands for the machine control system which is responsible for executing the quantum circuit, scheduling, and calibration routines. Automated calibrations take up about 25% of the system duty cycle and are either executed on a predetermined time interval or triggered when a measured parameter exceeds the specified tolerance. Clock synchronization between qubits is main-

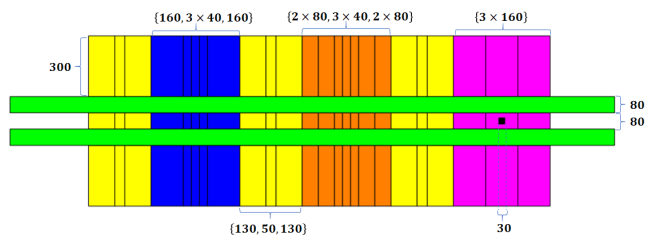


FIG. 4. Close-up schematic of the of trap. All dimensions are in μm . We refer to the blue gating region on the left as G1 and the orange gating region as G2.

tained via a phase-tracking protocol which updates the qubit phases after transport and gate operations to account for AC-Stark shifts.

Data corruption from background collisions causing ion loss or crystal reordering events are mitigated by probing the ion crystal mode structure. When these rare events are detected, the data since the previous check is discarded and the circuits are repeated. The mitigation procedure is blind to events that swap the qubit ions and processes involving multiple reordering events that leave the ions in the correct order immediately prior to the probe.

Trapping and Transport Operations: A hole in the trap (Fig. 4) allows neutral atoms from an effusive thermal source to enter the trapping region where they are photoionized and Doppler cooled using standard techniques [26] and then transported to a gate zone.

A 190V RF drive at 42.35 MHz provides radial confinement in the trap and DC voltages provide axial confinement (x -direction). The radial principal axes are at 45 degrees relative to the trap surface. The single Yb ion trap frequencies are $\{\omega_x, \omega_y, \omega_z\} = 2\pi\{0.97, 2.7, 2.8\}$ MHz, resulting in a $8 \mu\text{m}$ long four-ion crystal.

The transport primitives listed in Table II are constructed using a method similar to those described in Ref. [39]. Waveforms are solved for with a quadratic program that minimizes the voltage amplitudes while generating a potential whose derivatives are constrained in space and time. Specifically, linear transport programs specify a trap minimum moving along the RF null, swaps specify the orientation of the principle axes through time, and the split-combine operation is solved for by specifying a quartic potential term and its strength relative to a quadratic term. During the split operation, the quadratic terms changes from positive to negative, creating a double-well potential.

Transport sequences are determined using a heuristic algorithm to assign gating operations to specific zones and times. A parallel bubble sort algorithm determines the transport operations needed for the sorting, and the individual primitives are drawn from a library. Primitives in the library specify dynamic voltages applied to the electrodes from arbitrary waveform generators. The

Operation	Duration(μ s)	Axial heat	Radial heat
Intrazone shift	57.8	<1	<1
Interzone shift	282.6	<1	<1
Split/combine	128.2	0.5-1	<1
Swap	200.0	2	<4

TABLE II. Transport primitive library and associated durations and heating. For heating estimates we fit spin-flip data from a four ion crystal to a model that assumes all modes are at the same temperature. The fitted temperatures are then converted to units of MHz and reported in the table. The times shown do not include interpolation between different operations or small delays in the electronics, which increase the time for every operation by $\sim 10\%$. The interzone shift is a linear shift between the two gate zones, and an intrazone shift moves ions within a single gate zone by $110 \mu\text{m}$ for single qubit addressing.

waveforms are stitched together using an interpolation procedure to ensure voltage continuity. The superposition principle for voltages along with the linearity of the constraints guarantees that a linear interpolation between trapping potentials will also yield a valid trapping potential.

Transport waveforms are constructed using the electric field for each electrode computed with a 3D electrostatic simulation of the trap, but must be augmented to account for the presence of stray electric fields. The augmentation voltages, or shim voltages, are determined during calibration routines and added to the trapping voltages in gate zones to cancel out stray fields during the gate operations. Over the course of a day, the stray electric fields vary by up to a few tens of V/m.

Qubit Manipulation: We apply a 5G magnetic field at a 45° angle with respect to the trap axis which is uniform between the two zones to within 0.2 mG, ensuring that qubit frequencies are the same to within 1 Hz. The qubit coherence time is characterized by a single-pulse spin-echo sequence in the two zones, showing $1/e$ times of 2.0(2) s and 2.0(3) s for the first and second gate zones respectively. Lasers are directed into the gate zones at either 45 or 90 degrees to the trap axis and have a beam diameter of $\sim 17 \mu\text{m}$.

State preparation and measurement (SPAM): The qubits are initialized and measured using standard optical pumping and state-dependent fluorescence techniques [26], and the ions' fluorescence is imaged onto a linear PMT array for measurements.

The SPAM errors with 120 μs detection time listed in Table I are extracted from the y -intercept of the survival probability in single-qubit randomized benchmarking (RB). Theoretical modeling suggests the error from state preparation is $\leq 10^{-4}$, whereas the current photon collection efficiency should limit the measurement error to $> 10^{-3}$. Since these operations use resonant laser light, idle qubits are held at least $110 \mu\text{m}$ away during these op-

Operation	Duration(μ s)
Qubit initialization	10
Qubit measurement (high-fidelity)	120
Qubit measurement (low cross-talk)	60
Cooling stage 1 (Doppler)	550
Cooling stage 2 (Axial and Radial SB)	850
Cooling stage 3 (Axial SB)	650
Single-qubit $\pi/2$ time	5
Two-qubit gate	25

TABLE III. Qubit manipulation times. Circuits can be run using two different measurement protocols. For circuits where all measurements are made at the end, we use the high-fidelity measurement setting. Circuits containing mid-circuit measurements use shorter duration measurements to minimize the cross-talk error on idle qubits. The shorter detection time measurement error is $\sim 7 \times 10^{-3}$, about twice as large as those reported in Table I. Mid-circuit measurements induce an error of $\sim 1\%$ on neighboring idle qubits as measured by a Ramsey experiment. There are three different cooling stages used during transport (cooling stages 1 and 2) and before gates (cooling stage 3) and are either implemented through Doppler cooling or SB (sideband) cooling.

erations to avoid decoherence from scattered light. Measurement cross-talk errors are measured to be 0.35%-1.5% using the 60 μs detection time as explained in the caption of Table III while calculated errors from the detected ion's fluorescence at this separation are $< 10^{-3}$. A perfect Gaussian beam $110 \mu\text{m}$ away would give a $< 10^{-4}$ error and, therefore, we conclude the current limitations are due to imperfect beam profiles and scattering off the trap surface.

Gating operations: Quantum logic operations are accomplished via stimulated Raman transitions driven by two different configurations: single-qubit gates use pairs of co-propagating 370.3 nm Raman beams with circular polarization, and two-qubit gates use additional pairs of linearly polarized beams that couple to an axial mode of motion (along the RF null).

Single-qubit gates are characterized by performing single-qubit RB with each qubit following the standard Clifford-twirl version of RB outlined in Ref. [27], with results plotted for each qubit in Fig. 6a.

Two-qubit gates are characterized with two-qubit RB in each zone independently and then in both zones simultaneously [27]. Results are plotted in Fig. 6(b,c), and we report the average infidelity of the two-qubit Clifford gates scaled by the average number of U_{zz} gates per Clifford gate (1.5). The laser pulses that drive the Mølmer-Sørensen interaction use a $\sin^2(\frac{\pi}{2}t/T)$ envelope with $T = 1.5 \mu\text{s}$ for turning on and off to suppress unwanted spectator mode excitations. As indicated in Table IV, our models predict that two-qubit gate errors are dominated by position fluctuations of the ions stemming from voltage noise, introducing an effective phase noise source. Our estimate for the magnitude of this error uses

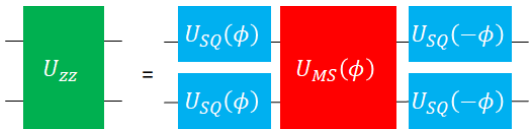


FIG. 5. Construction of a phase-insensitive two-qubit gate. The Mølmer-Sørensen interaction generates the unitary $U_{MS} = \exp(-i\frac{\pi}{4}(X\sin\phi + Y\cos\phi)^{\otimes 2})$ (red) whose basis is determined by the optical phase ϕ . Single-qubit operations driven by the same laser beams generate the unitary $U_{SQ} = \exp(-i\frac{\pi}{4}(X\cos\phi + Y\sin\phi))$ (blue) and are applied globally to both qubits. The resulting composite gate is, up to a global phase, given by $U_{zz} = \exp(-i\frac{\pi}{4}Z \otimes Z)$ (green).

Error Source	Magnitude(10^{-3})
Spontaneous emission	1.5
Debye-Waller	0.1
Trap frequency fluctuations	< 0.1
Laser phase noise	< 0.5
Spectator mode coupling	0.1
Position fluctuations (voltage noise induced)	5
Total	< 7.2

TABLE IV. An estimated error budget for the two-qubit gate operation.

the measured voltage noise spectral density and a numerically calculated phase noise filter function [40].

Simultaneous Randomized Benchmarking This method has two parts: (1) identify differences in RB decay rates between applying gates individually and simultaneously, and (2) identify correlated errors when applying gates simultaneously (also similar to Ref. [41]).

Two-qubit simultaneous RB is performed by three experiments: (1) RB in zone one, (2) RB in zone two, and (3) RB in both zones simultaneously. For reference, we fit the RB data to the decay equation $p(\ell) = A\alpha^\ell + B$ where $p(\ell)$ is the average survival frequency for a length ℓ RB sequence, A is the SPAM parameter, α is the RB decay rate, and B is the asymptote, which is fixed by randomization of the final measurement and the uncertainty is calculated via a semi-parametric bootstrap resample outlined in Ref. [24, 42, 43].

Addressability errors γ_z are induced in one zone from operations in the other zone and are quantified as the difference between the decay rates from experiments one and two, α_z for $z = 1, 2$, and the decay rates from experiment three, α_z^{both} [30],

$$\gamma_z = |\alpha_z - \alpha_z^{\text{both}}|. \quad (1)$$

We compare the decay rates instead of the fidelity, as done in Ref. [30]. As summarized in Table V, the measured values of γ_z are below 10^{-3} and within one standard deviation of zero.

Correlation errors are shared between zones when running RB simultaneously. Ref. [30] showed that corre-

Zone	α_z	α_z^{both}	γ_z
1	0.9866(9)	0.9856(8)	$9(10) \times 10^{-4}$
2	0.9820(8)	0.9824(8)	$4(12) \times 10^{-4}$

TABLE V. Addressability error estimates for simultaneous RB. The quantities α_z^{both} and γ_z refer to simultaneous RB decay rates and their deviation from individual RB decay rates as described in the text.

lated single-qubit errors can be identified by the outcomes in simultaneous RB experiments. The structure of the two-subsystem Clifford group $C_1^{\otimes 2}$ leads to three distinct decay rates, two corresponding to individual errors on each qubit and the other corresponding to correlated errors, which are estimated by measuring the Pauli observables $\langle \mathbb{1}Z \rangle$, $\langle Z\mathbb{1} \rangle$, and $\langle ZZ \rangle$. For parallel two-qubit gates, there are still three different decay rates for $C_2^{\otimes 2}$ but there are fifteen different Pauli observables. Six of these observables decay due to errors occurring separately on the two pairs of qubits. These are the Pauli operators with the identity acting on one of the qubit pairs, and at least one Pauli Z acting on the other qubit pair, labeled as $\beta_{z,i}$ for $z = 1, 2$ and $i = 1, 2, 3$. If standard RB assumptions hold, then $\beta_{z,i} = \alpha_z^{\text{both}}$ for all i . The remaining nine observables have at least one Pauli Z acting on each qubit pair and decay due to correlated errors between the two pairs of qubits, labeled as $\mu_{i,j}$. If there are no correlated errors then $\mu_{i,j} = \beta_{1,i}\beta_{2,j}$. The magnitude of correlation errors is quantified by

$$\delta_{i,j} = |\beta_{1,i}\beta_{2,j} - \mu_{i,j}|, \quad (2)$$

for all Pauli observables. The results are summarized in Fig. 7, which plots $\delta_{i,j}$ for all nine values. The minimum uncertainty is 4.1×10^{-4} over all correlation parameters, showing that they are within one standard deviation of zero.

Simultaneous two-qubit RB indicates that addressability and correlation errors are consistent with zero. However, there may be errors present that do not change the average fidelity of an RB experiment but still cause different effects in a quantum circuit. Our method does not capture all possible cross-talk errors, but it is a strong indication that these errors are minimal in this system. We note that this measurement indicates that cross-talk between interaction zones is negligible, but other modes of operation in which qubits are stored in auxiliary zones during gate operations require further characterization.

Teleported CNOT gate: The circuit for teleporting a CNOT gate is shown in Fig. 8a. Qubits q_1 and q_2 are prepared in the Bell state $\frac{1}{\sqrt{2}}(|00\rangle + |11\rangle)$, then distributed between the two zones through transport operations. Two rounds of CNOT gates (compiled into native U_{zz} and single-qubit gates) followed by measurements and conditional gates result in a circuit that is logically equivalent to a CNOT controlled on q_0 and targeting q_3

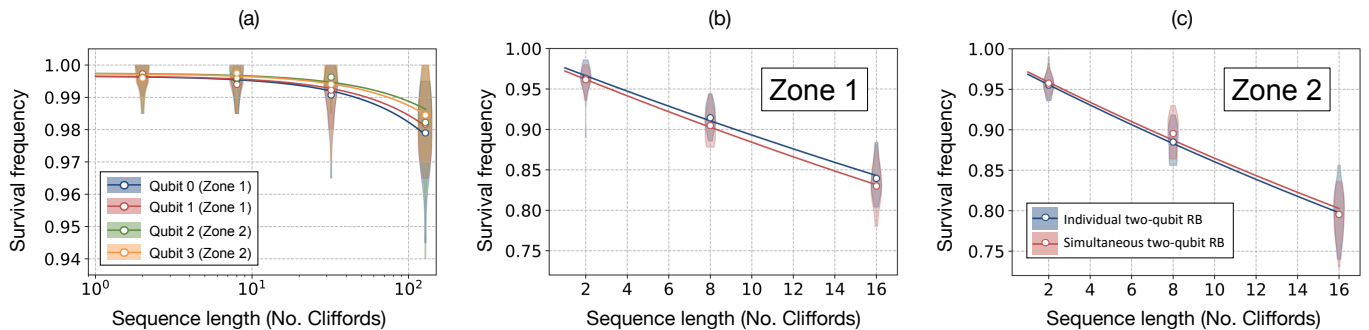


FIG. 6. Randomized benchmarking in the $N = 4$ mode. (a) Single-qubit randomized benchmarking for all four qubits. (b,c) Two-qubit randomized benchmarking results for both zones. We performed two-qubit randomized benchmarking in each zone, both separately and simultaneously, and observe no statistically significant difference between the two sets of experiments indicating that cross-talk errors do not play a significant role in our two-qubit gates.

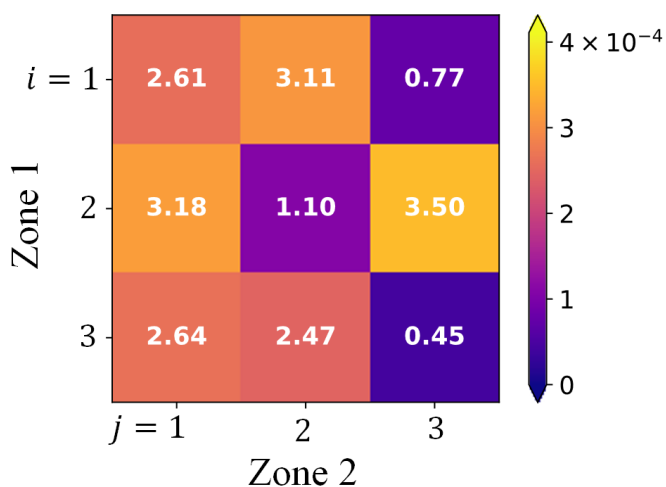


FIG. 7. Correlation parameters for simultaneous two-qubit RB. Each square represents a value of $\delta_{i,j}$ with the numbers being scaled by 10^{-4} , and all within one standard deviation of zero.

(see Fig. 8). A breakdown of the time budget for the circuit is shown in Fig. 9.

Benchmarking the teleported CNOT gate amounts to verifying the following quantum truth table [44]:

$$\begin{aligned}
 \text{CNOT: } & \begin{aligned}
 |00\rangle &\mapsto |00\rangle, & |++\rangle &\mapsto |++\rangle, \\
 |01\rangle &\mapsto |11\rangle, & |+-\rangle &\mapsto |+-\rangle, \\
 |10\rangle &\mapsto |10\rangle, & |-+\rangle &\mapsto |--\rangle, \\
 |11\rangle &\mapsto |01\rangle, & |--\rangle &\mapsto |+-\rangle,
 \end{aligned}
 \end{aligned}$$

where the states are labeled $|q_3 q_0\rangle$. We prepare q_0 and q_3 in each state of the $\{|0\rangle, |1\rangle\}$ and $\{|+\rangle, |-\rangle\}$ bases, apply the circuit in Fig. 8a and measure in the appropriate basis. The data is shown in Fig. 8b.

We define f_1 and f_2 as the average success probabilities over the $\{|0\rangle, |1\rangle\}$ and $\{|+\rangle, |-\rangle\}$ bases, respectively. The average fidelity F_{avg} [45] of the teleported CNOT gate is

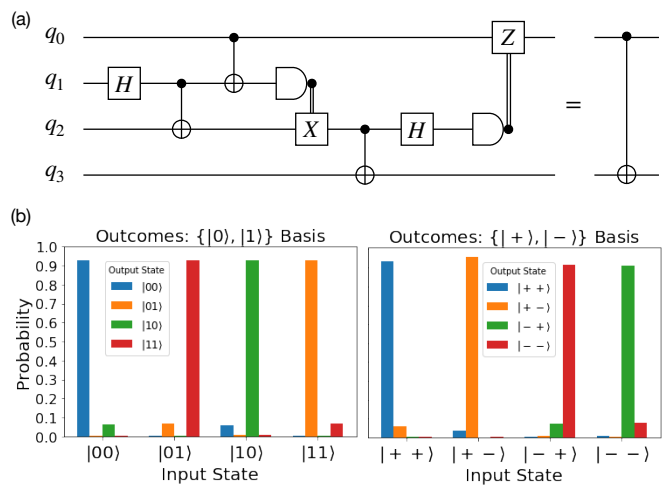


FIG. 8. Teleported CNOT circuit. (a) Circuit implementing a teleported CNOT gate, with q_0 and q_3 the control and target qubits, respectively. (b) Bar plots showing the distribution of measurement outcomes when qubits q_0 and q_3 are prepared and measured in the $\{|0\rangle, |1\rangle\}$ and $\{|+\rangle, |-\rangle\}$ bases.

lower bounded according to

$$F_{\text{avg}} \geq \frac{4}{5}(f_1 + f_2) - \frac{3}{5}. \quad (3)$$

This bound does not account for errors in the state preparations and measurements, but these errors are much smaller than the full circuit error. We find $f_1 = 0.933(6)$ and $f_2 = 0.941(5)$, yielding $F_{\text{avg}} \geq 0.899(6)$.

Quantum volume: The $N = 2, 3$, and 4 tests were performed with four qubit ions loaded into the machine, and the $N = 6$ test was performed with six qubit ions loaded into the machine. The $N = 2, 3$, and 4 tests consisted of 100 random circuits repeated 500 times each, and the $N = 6$ circuits consisted of 400 circuits repeated 100 times each, all generated by Qiskit [32]. All confidence intervals are calculated from the method in Ref. [7].

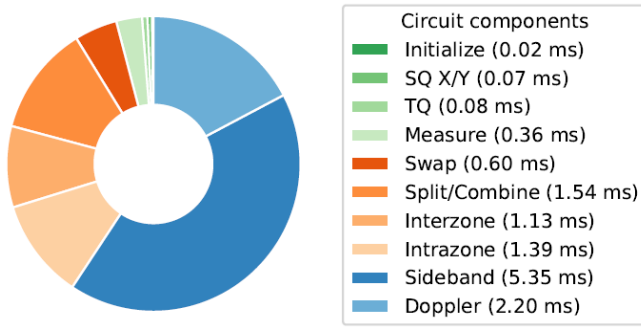
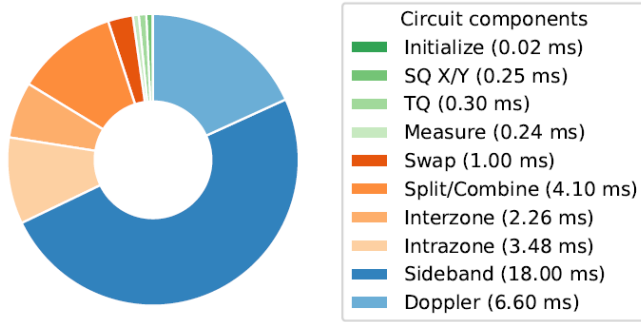


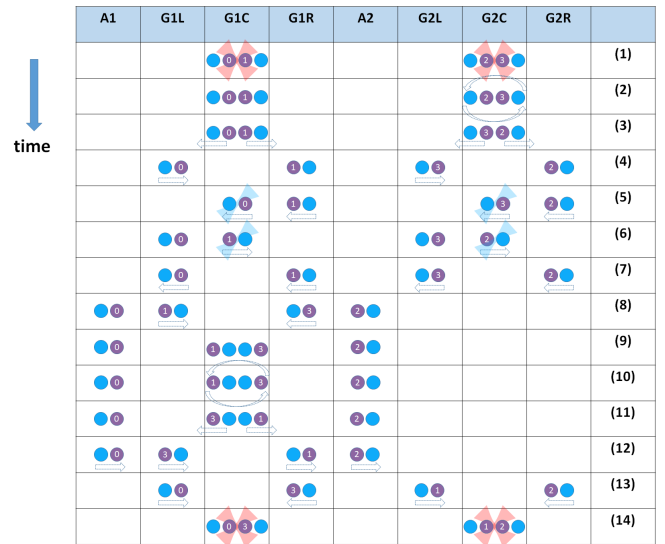
FIG. 9. The teleported CNOT gate time budget.

FIG. 10. The $N = 4$ QV test time budget.

The $N = 2, 3$, and 4 QV circuits were run without any optimization or approximations. For example, in the $N = 4$ test, each circuit contained exactly 24 two-qubit gates. Due to various initialization time overheads, we chose an accelerated $N = 6$ test that is optimized by combining single-qubit gates and $SU(4)$ gates when the random permutations allow it [7]. An example of the transport operations for the $N = 4$ case is depicted in Fig. 2.

* juan.pino@honeywell.com

- [1] Wineland, D. J. *et al.* Experimental issues in coherent quantum-state manipulation of trapped atomic ions. *Journal of Research of the National Institute of Standards and Technology* **103**, 259–328 (1998).
- [2] Kielpinski, D., Monroe, C. & Wineland, D. J. Architecture for a large-scale ion-trap quantum computer. *Nature* **417**, 709–711 (2002). URL <https://doi.org/10.1038/nature00784>.
- [3] Gaebler, J. P. *et al.* High-fidelity universal gate set for ${}^9\text{Be}^+$ ion qubits. *Phys. Rev. Lett.* **117**, 060505 (2016). URL <https://link.aps.org/doi/10.1103/PhysRevLett.117.060505>.
- [4] Ballance, C. J., Harty, T. P., Linke, N. M., Sepiol, M. A. & Lucas, D. M. High-fidelity quantum logic gates using trapped-ion hyperfine qubits. *Phys. Rev. Lett.* **117**, 060504 (2016). URL <https://link.aps.org/doi/10.1103/PhysRevLett.117.060504>.
- [5] Christensen, J. E., Hucul, D., Campbell, W. C. & Hudson, E. R. High fidelity manipulation of a qubit built from a synthetic nucleus (2019). URL <https://arxiv.org/pdf/1907.13331.pdf>. 1907.13331.
- [6] Wan, Y. *et al.* Quantum gate teleportation between separated qubits in a trapped-ion processor. *Science* **364**, 875–878 (2019). URL <https://doi.org/10.1126/science.aaw9415>.
- [7] Cross, A. W., Bishop, L. S., Sheldon, S., Nation, P. D. & Gambetta, J. M. Validating quantum computers using randomized model circuits. *Phys. Rev. A* **100**, 032328 (2019). URL <https://link.aps.org/doi/10.1103/PhysRevA.100.032328>.
- [8] Cirac, J. I. & Zoller, P. Quantum computations with cold trapped ions. *Phys. Rev. Lett.* **74**, 4091–4094 (1995). URL <https://link.aps.org/doi/10.1103/PhysRevLett.74.4091>.
- [9] Monroe, C., Meekhof, D. M., King, B. E., Itano, W. M. & Wineland, D. J. Demonstration of a fundamental quantum logic gate. *Phys. Rev. Lett.* **75**, 4714–4717 (1995). URL <https://link.aps.org/doi/10.1103/PhysRevLett.75.4714>.
- [10] Wang, Y. *et al.* Single-qubit quantum memory exceeding ten-minute coherence time. *Nat. Photonics* **11**, 646–650 (2017). URL <https://doi.org/10.1038/s41566-017-0007-1>.
- [11] Monroe, C. *et al.* Large-scale modular quantum-computer architecture with atomic memory and photonic interconnects. *Phys. Rev. A* **89**, 022317 (2014). URL <https://link.aps.org/doi/10.1103/PhysRevA.89.022317>.
- [12] Hucul, D. *et al.* Modular entanglement of atomic qubits using photons and phonons. *Nat. Phys.* **11**, 37–42 (2015). URL <https://doi.org/10.1038/nphys3150D0>.
- [13] Labaziewicz, J. *High Fidelity Quantum Gates with Ions in Cryogenic Microfabricated Ion Traps*. Ph.D. thesis, MIT (2008). URL <http://web.mit.edu/~cua/www/>

FIG. 11. An example of the transport operations needed in an $N = 4$ QV test circuit.

- quanta/LabaziewiczThesis.pdf.
- [14] Maunz, P. L. W. High optical access trap 2.0. *SAND2016-0796R* (2016). URL <https://prod-ng.sandia.gov/techlib-noauth/access-control.cgi/2016/160796r.pdf>.
- [15] Bowler, R. *et al.* Coherent diabatic ion transport and separation in a multizone trap array. *Phys. Rev. Lett.* **109**, 080502 (2012). URL <https://link.aps.org/doi/10.1103/PhysRevLett.109.080502>.
- [16] Kaushal, V. *et al.* Shuttling-based trapped-ion quantum information processing. *AVS Quantum Science* **2**, 014101 (2020). URL <https://doi.org/10.1116/1.5126186>.
- [17] Barrett, M. D. *et al.* Sympathetic cooling of ${}^9\text{Be}^+$ and ${}^{24}\text{Mg}^+$ for quantum logic. *Phys. Rev. A* **68**, 042302 (2003). URL <https://link.aps.org/doi/10.1103/PhysRevA.68.042302>.
- [18] Palmero, M., Bowler, R., Gaebler, J. P., Leibfried, D. & Muga, J. G. Fast transport of mixed-species ion chains within a paul trap. *Phys. Rev. A* **90**, 053408 (2014). URL <https://link.aps.org/doi/10.1103/PhysRevA.90.053408>.
- [19] Home, J. P. & Steane, A. M. Electrode configurations for fast separation of trapped ions. *Quantum Information and Computation* **6**, 289–325 (2006). URL <https://dl.acm.org/doi/10.5555/2012086.2012087>.
- [20] Splatt, F. *et al.* Deterministic reordering of ${}^{40}\text{Ca}^+$ ions in a linear segmented paul trap. *New Journal of Physics* **11**, 103008 (2009). URL <https://doi.org/10.1088/1367-2630/11/10/103008>.
- [21] Haberman, N. Parallel neighbor sort (or the glory of the induction principle). *CMU Computer Science Report* (1979).
- [22] Sørensen, A. & Mølmer, K. Entanglement and quantum computation with ions in thermal motion. *Phys. Rev. A* **62**, 022311 (2000). URL <https://link.aps.org/doi/10.1103/PhysRevA.62.022311>.
- [23] Lee, P. J. *et al.* Phase control of trapped ion quantum gates. *Journal of Optics B: Quantum and Semiclassical Optics* **7**, S371–S383 (2005). URL <https://doi.org/10.1088/1464-4266/7/10/025>.
- [24] Baldwin, C. H., Bjork, B. J., Gaebler, J. P., Hayes, D. & Stack, D. Subspace benchmarking high-fidelity entangling operations with trapped ions. *Phys. Rev. Research* **2**, 013317 (2020). URL <https://link.aps.org/doi/10.1103/PhysRevResearch.2.013317>.
- [25] Viola, L., Knill, E. & Lloyd, S. Dynamical decoupling of open quantum systems. *Phys. Rev. Lett.* **82**, 2417–2421 (1999). URL <https://link.aps.org/doi/10.1103/PhysRevLett.82.2417>.
- [26] Olmschenk, S. *et al.* Manipulation and detection of a trapped Yb+ hyperfine qubit. *Phys. Rev. A* **76**, 052314 (2007). URL <https://link.aps.org/doi/10.1103/PhysRevA.76.052314>.
- [27] Magesan, E., Gambetta, J. M. & Emerson, J. Scalable and robust randomized benchmarking of quantum processes. *Phys. Rev. Lett.* **106**, 180504 (2011). URL <https://link.aps.org/doi/10.1103/PhysRevLett.106.180504>.
- [28] Monroe, C. *et al.* Resolved-sideband raman cooling of a bound atom to the 3d zero-point energy. *Phys. Rev. Lett.* **75**, 4011–4014 (1995). URL <https://link.aps.org/doi/10.1103/PhysRevLett.75.4011>.
- [29] Jordan, E. *et al.* Near ground-state cooling of two-dimensional trapped-ion crystals with more than 100 ions. *Phys. Rev. Lett.* **122**, 053603 (2019). URL <https://link.aps.org/doi/10.1103/PhysRevLett.122.053603>.
- [30] Gambetta, J. M. *et al.* Characterization of addressability by simultaneous randomized benchmarking. *Phys. Rev. Lett.* **109**, 240504 (2012). URL <https://link.aps.org/doi/10.1103/PhysRevLett.109.240504>.
- [31] Eisert, J., Jacobs, K., Papadopoulos, P. & Plenio, M. B. Optimal local implementation of nonlocal quantum gates. *Phys. Rev. A* **62**, 052317 (2000). URL <https://link.aps.org/doi/10.1103/PhysRevA.62.052317>.
- [32] Abraham, H. & *et al.* Qiskit: An open-source framework for quantum computing (2019).
- [33] Mourik, M. W. v. *et al.* Coherent rotations of qubits within a multi-species ion-trap quantum computer (2020). URL <https://arxiv.org/pdf/2001.02440.pdf>. 2001.02440.
- [34] Mount, E. *et al.* Single qubit manipulation in a micro-fabricated surface electrode ion trap. *New Journal of Physics* **15**, 093018 (2013). URL <https://doi.org/10.1088/1367-2630/15/9/093018>.
- [35] Mehta, K. K. *et al.* Integrated optical multi-ion quantum logic (2020). URL <https://arxiv.org/pdf/2002.02258.pdf>. 2002.02258.
- [36] Kovalev, A. A. & Pryadko, L. P. Quantum kronecker sum-product low-density parity-check codes with finite rate. *Phys. Rev. A* **88**, 012311 (2013). URL <https://link.aps.org/doi/10.1103/PhysRevA.88.012311>.
- [37] Labaziewicz, J. *et al.* Temperature dependence of electric field noise above gold surfaces. *Phys. Rev. Lett.* **101**, 180602 (2008). URL <https://link.aps.org/doi/10.1103/PhysRevLett.101.180602>.
- [38] Nielsen, M. A. & Chuang, I. L. *Quantum Computation and Quantum Information* (Cambridge University Press, 2000).
- [39] Blakestad, R. B. *Transport of Trapped-ion Qubits within a Scalable Quantum Processor*. Ph.D. thesis, University of Colorado (2010). URL <https://www.nist.gov/system/files/documents/2017/05/09/blakestad2010thesis.pdf>.
- [40] Biercuk, M. J., Doherty, A. C. & Uys, H. Dynamical decoupling sequence construction as a filter-design problem. *Journal of Physics B: Atomic, Molecular and Optical Physics* **44**, 154002 (2011). URL <https://doi.org/10.1088/0953-4075/44/15/154002>.
- [41] Harper, R., Flammia, S. T. & Wallman, J. J. Efficient learning of quantum noise (2019). URL <https://arxiv.org/pdf/1907.13022.pdf>. 1907.13022.
- [42] Meier, A. M. *Randomized Benchmarking of Clifford Operators*. Ph.D. thesis, University of Colorado (2006). URL <https://arxiv.org/abs/1811.10040>. 1811.10040.
- [43] Harper, R., Hincks, I., Ferrie, C., Flammia, S. T. & Wallman, J. J. Statistical analysis of randomized benchmarking. *Phys. Rev. A* **99**, 052350 (2019). URL <https://link.aps.org/doi/10.1103/PhysRevA.99.052350>.
- [44] Hofmann, H. F. Complementary classical fidelities as an efficient criterion for the evaluation of experimentally realized quantum operations. *Phys. Rev. Lett.* **94**, 160504 (2005). URL <https://link.aps.org/doi/10.1103/PhysRevLett.94.160504>.
- [45] Nielsen, M. A. A simple formula for the average gate fidelity of a quantum dynamical operation. *Physics Letters A* **303**, 249–252 (2002). URL [https://doi.org/10.1016/S0375-9601\(02\)01272-0](https://doi.org/10.1016/S0375-9601(02)01272-0).

Acknowledgements

This work was made possible by a large group of people, and the authors would like to thank the entire Honeywell Quantum Solutions team for their many contributions.

Competing Interests

The authors declare that they have no competing financial interests.

Correspondence

Correspondence and requests for materials should be addressed to david.hayes@honeywell.com.